

# A Modular and Self-Contained Fluidic Engine for Soft Actuators

Michael A. Bell,\* Benjamin Gorissen, Katia Bertoldi, James C. Weaver, and Robert J. Wood

Fluidic actuation in soft robots traditionally requires a complex assemblage of pumps, regulators, valves, and sensors, often resulting in large and bulky support systems. This added bulk can often hinder a robot's ability to be untethered, perform complex tasks, or bring challenges when it comes to maintenance or upgradeability. To address these limitations, herein, a simple and highly modular bidirectional soft robotic appendage is presented that integrates the pump, flow lines, and actuator into a compact, closed hydraulic system, which is driven by an integrated stepper motor, allowing for positional control and fast response times. The actuator can also be swapped in under five seconds, allowing for rapid reconfiguration. Each component has been thoroughly characterized to determine an overall electrical to mechanical efficiency of the system, and from these calculations, it is demonstrated that the actuator utilizes only 1/15th the required energy to achieve a specific bending angle, and is four-fold more power-efficient than similar-sized soft actuators and pumping systems reported in the literature. The integrated actuator and fluidic engine construct presented here thus represents a major departure from previous soft actuator control platforms in that everything is simplified down to a single self-contained unit, demonstrating unparalleled versatility and modularity.

rapid prototyping options for quickly exploring novel gaits or multilegged configurations.<sup>[10–15]</sup> In contrast, soft robotic prototypes that focus on the integration of customized fluidic systems with their adjacent actuators can offer the potential for increased actuator performance, longer autonomous range, and a more compact form factor.<sup>[16–20]</sup>

In an effort to simplify these traditionally complex, bulky, and inefficient fluidic power systems, here we describe the design and fabrication of a compact and fully self-contained peristaltic pump-based fluidic engine with an integrated bidirectional PneuNet actuator (Figure 1). Using a highly customizable manufacturing approach, this fully integrated soft robotic appendage can be fabricated with an embedded peristaltic pump cap, tubing, strain-limiting wire mesh, and removable chamber-defining soft cores, all while being fabricated in a simple one-step injection molding process, with no entrapped air bubbles.

## 1. Introduction

Consisting of dozens of separate and potentially error-prone components, modern soft robotic prototypes can exhibit staggeringly complex networks of tubes, pumps, valves, and sensors that are required for their successful operation.<sup>[1–9]</sup> As a consequence of this multicomponent complexity, most soft robots are bulky and inefficient, are difficult and time-consuming to service and upgrade, exhibit limited modularity, and offer limited

For the design of soft actuators, there are several pros and cons that must be considered when deciding whether to use pneumatic or hydraulic control systems. Gases are routinely used to power soft robots, and with low-cost compressors, valves, and tubing, are by far the most economical.<sup>[21,22]</sup> Gases have the advantage of being able to be stored at high pressure, so compressor-based systems only have to run a fraction of the time to store the required energy needed for actuation. There are, however, inherent efficiency losses in any compressed-gas-based system, as a portion of the energy powering the compressor is dissipated as heat. Depending on the application or intended environment, buoyancy from gases can assist a robot (e.g., for buoyancy control) or be detrimental when used under high hydrostatic pressures (e.g., for deep-sea applications).<sup>[17,23]</sup> Although actuator response times from gases are rapid, precise gas-actuated control requires sensors and feedback systems. Liquids, in contrast, are for all practical purposes incompressible, and in the right applications, lead to improved dynamic behavior, and higher efficiency as there is no energy loss due to fluid compression.<sup>[16,24]</sup> The liquid response time, however, is limited by cavitation, but its control can be significantly more precise than for gas-based systems.<sup>[25,26]</sup>

M. A. Bell, B. Gorissen, K. Bertoldi, J. C. Weaver, R. J. Wood  
Harvard Microrobotics Laboratory  
Harvard John A. Paulson School of Engineering and Applied Sciences  
150 Western Avenue, Allston, MA 02134  
E-mail: bell@seas.harvard.edu

The ORCID identification number(s) for the author(s) of this article can be found under <https://doi.org/10.1002/aisy.202100094>.

© 2021 The Authors. Advanced Intelligent Systems published by Wiley-VCH GmbH. This is an open access article under the terms of the Creative Commons Attribution License, which permits use, distribution and reproduction in any medium, provided the original work is properly cited.

DOI: 10.1002/aisy.202100094

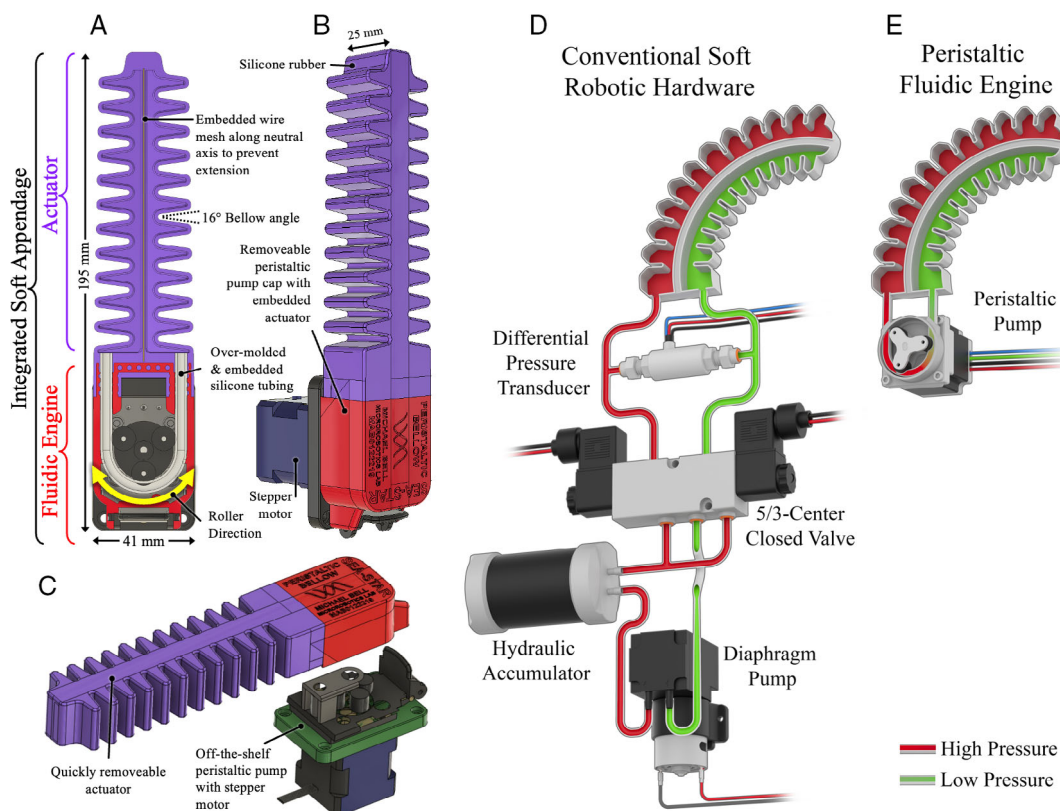


**Figure 1.** Design elements of the integrated soft robotic appendage. A–C) Schematic diagram of an integrated soft robotic appendage that combines a symmetrical bidirectional bellow actuator and a peristaltic pump. A) Top section view showing the peristaltic motor assembly, tube routing, cap features, and embedded metal mesh. B) Isometric 3D view showing the relative thicknesses of the different components. C) Demonstrated modularity of the bellow actuator and peristaltic pump assembly, which is completely self-contained, and can be removed/swapped within seconds. D, E) Hardware complexity in soft robotic power and control systems. D) Traditional schematic for controlling a bidirectional bellow actuator requiring high and low pressures. This method employs two five-way valves, a high pressure accumulator, and a digital pressure and vacuum gauge, which is mapped to position through electrical control. E) Integrated positive displacement pump schematic showing the need for just one stepper-motor-driven peristaltic pump to drive the entire system.

### 1.1. Limitations in Existing Fluidic Engines

During the prototyping process, we identified a set of fluidic engine design requirements for the successful operation of our bidirectional PneuNet actuator: 1) adequate flow rate and pressure to fully bend the actuator; 2) reversible (i.e., bidirectional) flow control; 3) zero static backflow or leakage between adjacent actuator bellows; 4) sensor-free positional control with achievable accuracies similar to that obtained from using a pressure sensor; 5) minimal fluid volume in the peripheral flow lines; and 6) response times similar to position-controlled pneumatic actuators (up to  $36^\circ \text{ s}^{-1}$ ).

To meet all of these design criteria, a range of fluidic engines was considered all of which could generally be categorized as either stored high-pressure fluid systems or microcompressors.

To achieve high pressures ( $>10 \text{ MPa}$ ) or high flow rates ( $>100 \text{ SLM}$ ), liquid  $\text{CO}_2$  or compressed air canisters can be used.<sup>[17,18,22]</sup> These canisters are beneficial in applications that only require positive pressure, and can be used in an antagonistic actuator pair.

Pressure pumps are also commonly used in these systems and allow ambient fluid to be compressed through the use of electric

motors or internal combustion engines (although other methods have also been demonstrated).<sup>[27,28]</sup> Pump types include micro-compressors, centrifugal, diaphragm, peristaltic, piston, screw, and vane-based designs. Batteries typically power on-board pumping systems, although liquid fuel can also be used, and a number of untethered robots with a wide range of body plans has been successfully developed using these approaches.<sup>[2,7,10,16,29]</sup>

Although diaphragm and centrifugal pumps are most often used due to their compact size (fist sized or smaller), low cost (sub-\$100), and useful operating pressure range up to  $0.2 \text{ MPa}$ , both pump types are not capable of running in reverse, and centrifugal pumps cannot prevent fluid backflow in a static state. As a result, most soft robots using these pump types also use valves, or include a second pump to handle stationary or reverse flows. Although previous studies have compared the energy density of these different soft robotic actuation systems as a function of weight, these calculations do not typically take into consideration the mass of all the necessary hardware for the system to function (tubes, valves, regulators, storage, sensors, etc.).<sup>[22]</sup>

For the application presented here, a peristaltic pump met all of our requirements. Many can achieve pressures up to  $\approx 100 \text{ kPa}$ , with flow rates determined by tube diameter and

motor speed. They are easily capable of forward or reverse operation and while pinching the tube to prevent backflow, and when combined with a stepper motor, allow for compact size and positional control.

Peristaltic pumps, however, are not commonly used in soft robotic applications due to the limited hydraulic power per unit volume or increased weight compared to equivalently sized diaphragm or centrifugal pumps.<sup>[22]</sup> This common lack of peristaltic pump implementation in traditional soft robotic fluidic networks is based on the fact that these systems tend to use an accumulator and a valving system to centrally distribute fluid to multiple actuators, instead of dedicating a single pump to each actuator. Despite these limitations, however, highly optimized actuators and fluidic systems, such as the positive displacement cyclic actuator developed by Katzschmann et al. for a robotic fish tail, are able to utilize the hydraulic fluid in a fully closed system, without the need for an accumulator, thereby

reducing weight and eliminating the need for other bulky fluidic components.<sup>[16]</sup>

Inspired by these previous integrated actuator-based systems, we set out to create a highly modular and more energy-efficient alternative. The key design elements of our fully integrated soft robotic appendage (**Figure 1**) are described in detail as follows. To eliminate the need for bulky barbed fittings, we began by spatially constraining the tubing within the pump housing, which reduced the dead volume of fluid in the tube to just 0.4% of the total system volume by placing the pump head adjacent to the actuator. We eliminated the need for an accumulator by utilizing the actuator's elastomeric properties within a closed system. We eliminated all valves by using a bidirectional pump that has no static backflow up to 100 kPa. We further eliminated the need for differential pressure feedback for positional control by using a stepper motor matched to a pump head designed for precision dosing. Through the implementation of these novel design elements into a fully integrated closed and easily

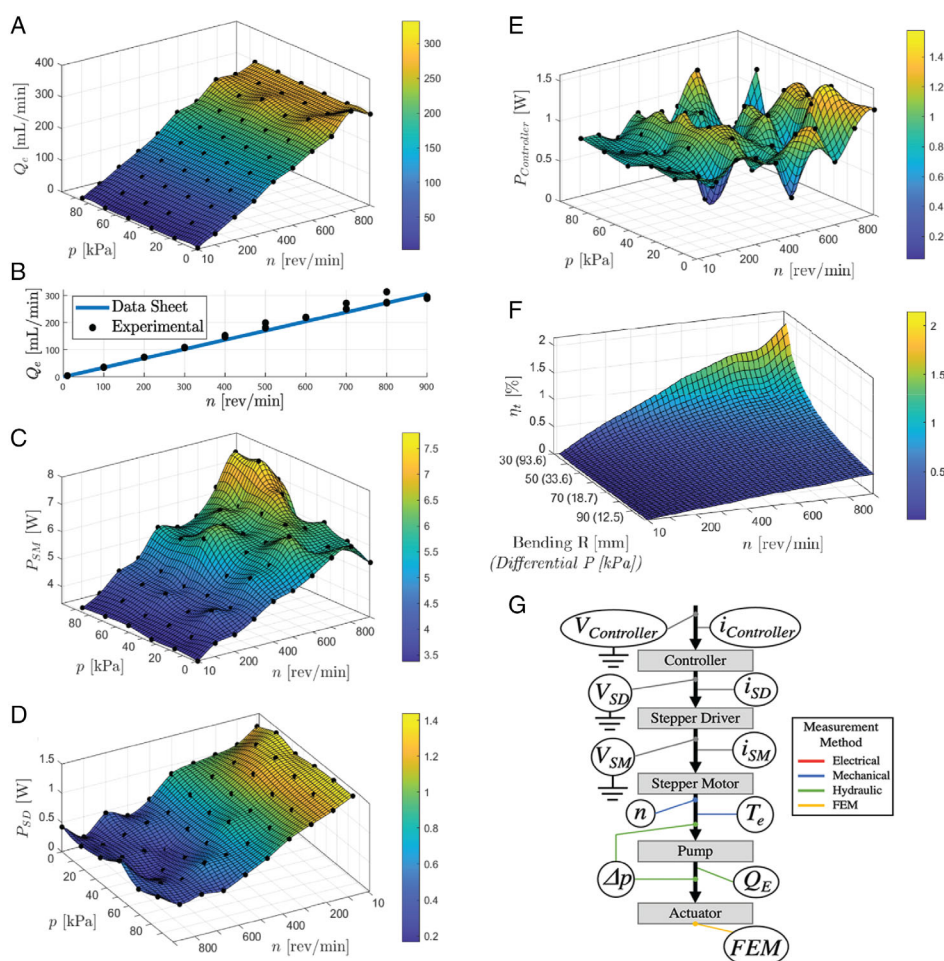


**Figure 2.** Performance quantification of the peristaltic pump using biharmonic interpolation. Solid black dots refer to experimental data points, with a surface plot fit to show trends. A) Results of the peristaltic pump volumetric displacement per revolution at varying angular velocities.  $Q_e$  is the effective volumetric flow rate of the peristaltic pump,  $p$  is the differential pressure of the pump, and  $n$  is the rotational velocity. B) A comparison of experimental flow rate with the pump technical specifications as provided by the manufacturer. C) Characterization of the stepper motor power,  $P_{SM}$ . D) The stepper driver's power,  $P_{SD}$  (note that the  $p$  and  $n$  axes are flipped compared to the other plots to better show the surface). E) The controller's power consumption,  $P_{Controller}$ . F) Overall system efficiency of the fluidic engine. G) Measurement schematic showing how the electrical, mechanical, hydraulic, and finite element modeling (FEM) measurements contribute to the overall efficiency.

swappable system, we have achieved a level of design simplicity, modularity, control, and fast response time not seen in traditional soft robotic prototypes.

## 1.2. Pumping, Storage, Control, and Feedback

Figure 1D displays a traditional minimalist closed hydraulic system to drive a bidirectional hydraulic actuator. A standard liquid rotary diaphragm pump is used with a hydraulic accumulator for the storage of pressurized fluid (similar to that of an electrical capacitor). A 5/3-closed center valve controls three states for each side of the actuator: inflation, stasis, and deflation. Once the actuator begins to inflate, (unloaded) curvature control can be achieved through reading the differential pressure gauge, which is mapped to the curvature of the entire actuator. If positional control is desired with a load, a strain sensor along the surface of the actuator, or pressure/force sensors along the surface, would be required to know where the external loads are being applied.

In contrast, our design shown in Figure 1E focuses on the unique abilities of a peristaltic pump. These types of pumps entrap a fixed amount of fluid per revolution, and a stepper motor allows precise volumetric control of the fluid, even with open-loop control. They are capable of reversing the flow direction simply by reversing the motor rotation, and naturally prevent backflow when idled, with the rotors pinching the tube in one or more positions. Peristaltic pumps can generate moderate

pressures (around 100 kPa), are self-priming, and as such, are generally chosen for precise dispensing applications, rather than for high flow rates. As shown in Figure 1E, our highly simplified hydraulic system is condensed to a single peristaltic pump driving the left and right bellow cavities directly.

## 2. Results

As shown in Figure 2F, the maximum system efficiency was  $\approx 2\%$ , with the smallest bending radius and highest differential pressure ( $R = 32$  mm at 86.2 kPa) obtained with a pump speed of 900 RPM. If we compare our results to those reported previously by Padovani et al. for a similar system configuration that incorporated a positive-displacement external gear micropump, our design exhibits a four-fold improvement in efficiency at equivalent RPM and pressure (900 RPM and 90 kPa).<sup>[24]</sup>

Figure 2A details the effective flow rate of the peristaltic pump,  $Q_e$ . Here we see the benefits of a positive displacement pump, where the volumetric displacement per revolution is fairly consistent over the full range of pressures. Although the experimental flow measurements we obtained are within  $\approx 15\%$  of those stated by the manufacturer, these minor deviations can likely be attributed to minor differences in tube material, tube wear, lubrication, pumping fluid type, and operating temperature.

In Figure 2A–E we evaluate  $P_{SM}$ ,  $P_{SD}$ , and  $P_{Controller}$ . We observe that the stepper motor's baseline power consumption

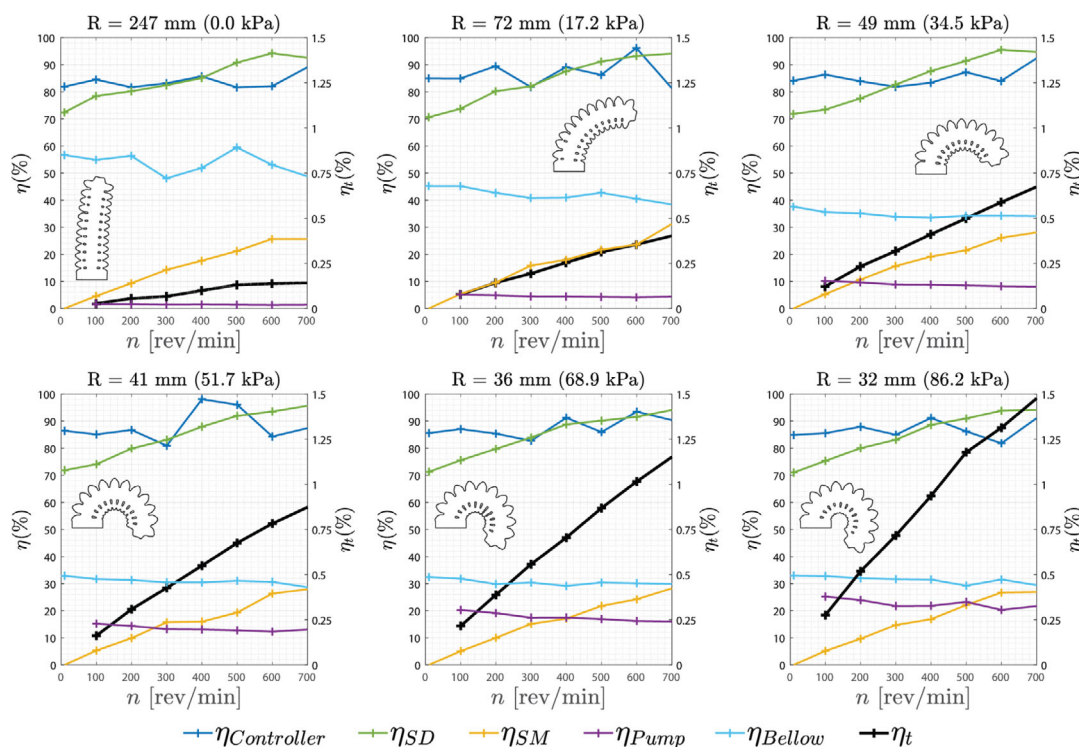


**Figure 3.** Efficiencies as a function of radius (or pressure) throughout a motor sweep from 10 to 700 RPM. The vertical axis,  $\eta(\%)$ , is the efficiency of the given system, with the left vertical axis for all subsystems, and the right vertical axis for the total system efficiency. The horizontal axis,  $n$ , is the rotational velocity of the stepper-motor-driven peristaltic pump. Each plot shows the efficiencies of all the components at a given actuator radius, starting at  $R = 247$  mm and ending at the minimum radius,  $R = 32$  mm. All six system efficiencies are listed in their respective colors, with the Duet 2 Wifi Controller,  $n_{Controller}$ , stepper driver,  $n_{SD}$ , stepper motor,  $n_{SM}$ , peristaltic pump,  $n_{PumpP}$ , bidirectional bellow,  $n_{Bellow}$ , and the total system efficiency  $n_t$ .

is  $\approx 3.5$  W at 10 RPM, and at full  $n$ , peaks at 7.5 W, as shown in Figure 2C. As expected, the stepper driver power consumption,  $P_{SD}$ , is inversely proportional to the RPM between 0.5 and 1.5 W, as shown in Figure 2D (note that the graph axis values are reversed compared to the other figures). Finally,  $P_{Controller}$  (Figure 2E) shows a relatively noisy plot but, in general, shows no obvious trend and is roughly constant within the operational ranges recommended by the manufacturer.

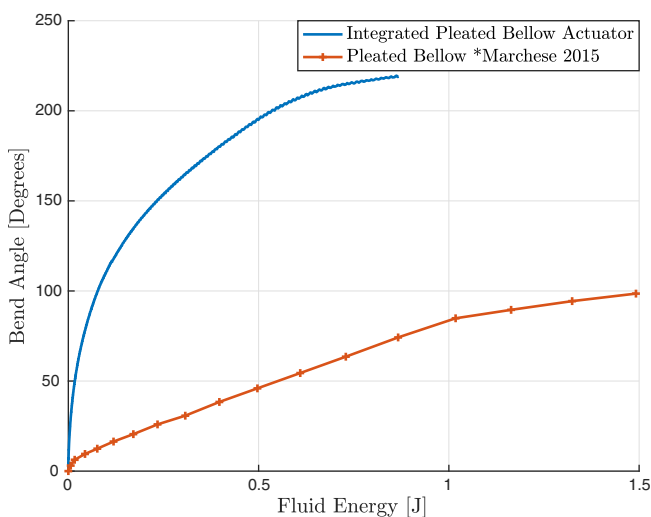
Six pressure and radius of curvature values are plotted in Figure 3, showing changing curvature as the bellow actuates from near rest ( $R = 247$  mm/0 kPa) to fully curved (32 mm/86.2 kPa). For reference, Table 1 includes achievable numerical ranges for each subsystem.

Figure 3 shows the key efficiency data at six notable bending radii. These estimates clearly demonstrate that efficiency is mainly limited by  $n_{SM}$  and  $n_{Pump}$ , which are directly correlated to RPM and differential pressure as described by Equations (S3.4) and (S3.6), Supporting Information, respectively.  $n_{Bellow}$  is the third limiting factor and is directly correlated to the energy expended during the deformation of the bellow's elastomeric material.

Because, to our knowledge, there is no existing information regarding whole system efficiency for soft robotic appendages (from electrical input power to mechanical output power), we can take a compartmentalized approach for comparing the performance metrics of our system to similar bellow actuators described previously.<sup>[19]</sup> Figure 4 compares Marchese et al.'s bellow design to our own, both

**Table 1.** Efficiency ranges of all subsystems.

	Efficiency range	
	Min	Max
$\eta_{Controller}$	0.810	0.981
$\eta_{SD}$	0.706	0.957
$\eta_{SM}$	$\leq 0.001$	0.312
$\eta_{Pump}$	0.013	0.252
$\eta_{Bellow}$	0.287	0.595



**Figure 4.** Performance comparison between the actuator described in this study and a similar design reported previously by Marchese et al.<sup>[19]</sup>

**Table 2.** Pleated actuator comparison.

	Integrated pleated bellow	Pleated bellow (Marchese 2015)
Actuator length [mm]	125.0	107.5
Actuator width [mm]	38.7 <sup>a)</sup>	44.4
Actuator thick. [mm]	25.0	25.4
No. of channels per side	12	10
Single channel length [mm]	10.0	12.9
Single channel width [mm]	14.2 <sup>a)</sup>	12.3
Single channel thick. [mm]	3.1 <sup>a)</sup>	2.8
Cavity volume per side [mL]	19.2 <sup>b)</sup>	5.12

<sup>a)</sup>Average value based on drafted geometry; <sup>b)</sup>Does not include volume in peristaltic tubing.

of which exhibit similar dimensions and operating pressures, as shown in Table 2. As seen from these comparative studies, our bellow is capable of nearly double the bending angle, for only half the required pumping energy, results which may be related to minor design element differences, including bellow angle, wall thickness, and width of the central axis, between the two systems.

### 3. Conclusion

In this study, we have designed a modular soft robotic appendage that integrates a bidirectional PneuNet actuator and a peristaltic pump into a high-efficiency and quickly swappable fully self-contained unit. This simplified design eliminates the need for regulators, valves, sensors, and the majority of tubing seen in traditional soft robots, while simultaneously achieving a compact, tunable closed fluidic system with a sub-4 s bending time from 0 to 135° (at 900 RPM). Our characterization and comparisons to other soft robotic prototypes utilizing positive displacement pumps demonstrate that our design requires only 1/15th the required energy to achieve a specific actuator bending angle, and exhibits an overall fourfold increase in power efficiency.

Although the goal of this study was focused on the development of a highly efficient soft robotic appendage using inexpensive off-the-shelf components, future iterations could also use custom-manufactured elements for achieving increased efficiency for task-specific applications. These improvements in efficiency and actuation speed would mainly come from increasing the peristaltic pump's volumetric flow rate. As shown in Figure 2F, the higher the RPM of the motor (which translates to a higher volumetric flow rate), the higher is the efficiency of the overall system, which could be achieved through a number of methods, including 1) increasing the inner diameter of the tubing, thereby increasing the volumetric displacement per revolution of the peristaltic pump rollers. This modification would, however, reduce the positional accuracy of the peristaltic pump, which currently has a very precise resolution of 21.3  $\mu$ L (does not include volume in peristaltic tubing), for an overall actuator volume of 26 mL. 2) Increasing the diameter of the three-peristaltic-roller assembly (and tube contact arc), which will, in turn, increase the fluidic volumetric flow rate. This modification would, however,

reduce the positional accuracy of the system, and also limit the maximum motor speed, up to either a motor torque or fluid cavitation limit. 3) Increasing the motor speed, which would require a different stepper motor, or replacement of the stepper motor with a DC motor and encoder. This modification could also entail adding a gear box to the stepper motor to increase the RPM, while reducing torque, which could directly increase the volumetric flow rate of the fluid, up to either its torque or fluid cavitation limit.

Because of its highly modular and self-contained architecture, we envision that our integrated soft appendage could be used for the rapid development of application-specific soft robots designed to navigate a wide range of different terrains.

Since the self-contained fluidic engine directly translates electrical signals into bellow movement through a closed fluidic system, retrofitting existing robotic arms would not require additional plumbing or the installation of additional pneumatic or hydraulic hardware.

Further refinements to our design to favor specific performance metrics, such as applied load or minimum bending radius of curvature, could provide the basis for a set of performance-optimized and geometrically standardized components for a soft robotic toolkit, where fully interchangeable elements could be tiled together and quickly exchanged to explore task-specific gaits or manipulator configurations.

As such, this fluidic engine could be used in the development of multifinger grippers with interchangeable units for shape-specific grasping, or in the prototyping of new robotic platforms such as the example shown in **Figure 5**, where five of these appendages are arranged in a radially symmetrical echinoderm-inspired architecture.

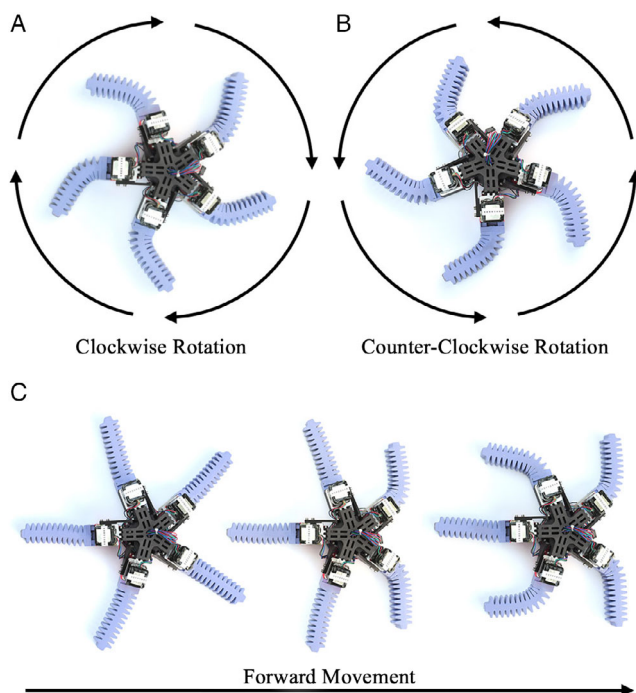


**Figure 5.** Conceptual photographs of an echinoderm-inspired architecture that integrates our bidirectional actuators in an agile pentaradial configuration. Potential robot gaits: A) clockwise, B) counterclockwise rotation, and C) a sequential rowing-like gait to achieve forward movement.

As demonstrated by these examples, the fully integrated soft appendage described here thus offers several unique opportunities for the creation of more energy-efficient multifinger and multilegged robotic prototypes that exhibit intrinsic robustness and high modularity, and helps lay the groundwork for the design and development of customized task- and environment-specific soft actuators and fully adaptable, customizable, and versatile robotic research platforms for a wide range of emerging applications.

## 4. Experimental Section

**Bidirectional PneuNet Actuator Integration:** Although traditional soft, pleated, PneuNet actuators are designed to have maximum curvature in one direction, which is induced by a positive pressure differential, limited bending can also be achieved in the opposite direction by applying a vacuum. This reverse bending is highly limited by the angle of the bellow segments (as shown in Figure 1), where a bellow angle close to zero corresponds to minimal bending. As the bellow angle increases, the amount of reverse bending also increases, which can be effectively leveraged when designing a bidirectional actuator, consisting of back-to-back PneuNet bellows, which were used in this study. As shown in Figure 1E, one of the major advantages of using a peristaltic pump for controlling the bending of a bidirectional PneuNet actuator is that during pumping, the convex actuator is inflated, while the concave actuator is simultaneously evacuated, both at constant rates, significantly reducing bending resistance, increasing efficiency, and minimizing achievable bending radius.

**Design:** The actuator was designed to integrate directly into the removable cap of a peristaltic pump. The two main factors for pump selection included a pumping rate that could achieve the desired bending rate of the actuator and the maximum achievable pressure differential. In addition, there were other peristaltic pump-specific design features that needed to be explored that could directly influence system performance. For example, although fewer tube rollers in a peristaltic pump would reduce the volumetric flow rate, this modification would reduce the resolution of the volumetric flow control. To thus explore these trade-offs in an application-specific context, the ability to swap out rotors with different roller quantities was a key consideration. To meet the aforementioned performance metrics, a Boxer 9QQ pump (Boxer GmbH, Ottobereun, Germany) was selected due to its robust and removable cap system, U-shaped tube routing design, a configurable number of rollers (3/4/6 rollers corresponding to 400/340/230  $\mu$ L per revolution), and motor selection options (AC versus DC, and traditional versus stepper). After extensive evaluation of these different pump options, a high flow rate, three roller, stepper motor version was chosen for the final design (Boxer 9600.930).

A common challenge with the fabrication of fluidic elastic actuators and soft robots is the robust connection of the soft and rigid components. In the example discussed here, a method was needed by which a robust connection could be created between the soft fluidic elastic actuators and the rigid cap of the Boxer 9QQ peristaltic pump. To increase the available surface area for bonding and to distribute potential interfacial stresses between the modulus-mismatched components, a modified cap (shown in Figure 1 and 6), was designed with a 14.0 mm  $\times$  38.5 mm  $\times$  22.5 mm porous region along the connecting edge, consisting of 2.0 mm diameter holes spaced 4.0 mm on center, and arranged in a square grid pattern. During the fabrication process, high-pressure injected silicone impregnated this region and formed a robust mechanical connection between the two materials.

Typical PneuNet actuators frequently incorporate an inextensible fiber or mesh to favor bending overextension during inflation. Although there are many different materials that are likely suitable for such applications, fabrics such as cheesecloth have fibers that are challenging to restrain during molding, limiting fabrication reproducibility. To eliminate problems encountered through the use of cloth fibers, a thin metal mesh

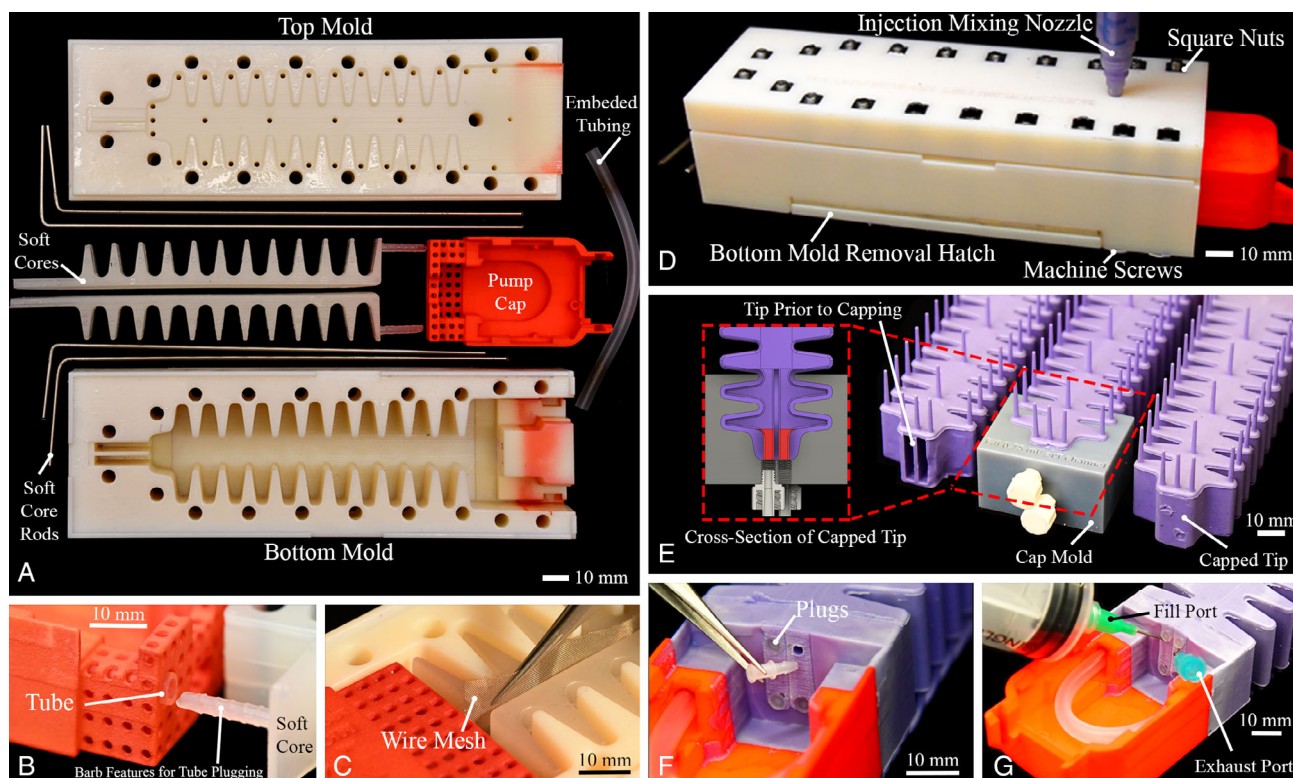


**Figure 6.** Major manufacturing steps of the integrated soft appendage. A) Overview of all parts used, including top and bottom molds, two soft cores, four 2.0 mm diameter stainless steel rods to suspend the cores, a modified 3D-printed pump cap, and a segment of 5.0 mm OD  $\times$  3.0 mm ID silicone tubing. B) Plug feature of the soft core prior to insertion into the tubing (which had been inserted into the modified pump cap). C) Insertion of the wire mesh down the actuator's neutral axis. D) Injection molding the static mixing nozzle into the gate of the mold. E) An additional step is needed to seal the actuator's tip after the soft cores have been removed, from left to right: open cavity of the soft core after removal, cap mold with Luer lock fittings to inject a specific volume (0.75 mL) of elastomer into each cavity while hanging vertically, and the final result when the cap is removed and the flashing is trimmed. Cross-sectional schematic (left) showing filled material in red, fill ports in white, and the surrounding mold in gray. F) Insertion of 1/8" diameter polypropylene plugs to seal the bellow under the cap. G) Filling the actuator with water was performed by inserting small needles between the plug and the hole, with the green nozzle injecting water and the aqua nozzle allowing air to escape. Once all air escaped, the blue nozzle was removed and the bellow was pressurized, and finally, the green nozzle was removed.

(RadioScreen, Less EMF Inc., Latham, NY, USA) was inserted down the full length of the neutral axis, as shown in Figure 6C.

Another fabrication challenge was the comolding of the tube through the peristaltic pump cap, and into the actuator. To resolve this issue, a modified cap was created to hold a small length of tubing while slightly pinching it near the cut ends to reduce the likelihood of pull-out during pumping. A number of tube materials were evaluated for robust adhesion to Smooth-Sil 945 (Smooth-on, Macungie, PA, USA), and platinum-cured silicone tubing manufactured for Boxer Pumps (Boxer 9000.508) was eventually selected for its highest adhesion strength to the elastomer.

To produce the integrated soft appendage in a single fabrication step, a high-pressure liquid silicone injection molding process was used. To create the internal cavities within the actuator, removable soft cores<sup>[23]</sup> were suspended inside the mold using 2 mm stainless steel rods, which protruded through the exterior mold on both sides. The two soft cores (for the right and left internal bellows) also contained a ribbed plug-like feature that was inserted into two ends of the tubing, which created seals and prevented the liquid silicone from ingress. The outer mold was produced on a Connex500 3D printer (Stratasys, Eden Prairie, MN, USA) using VeroClear (RGD810) material. The modified pump cap was produced on an HP Multijet Fusion printer from thermally sintered nylon (HP Inc., Palo Alto, CA). The mold was designed with an injection gate

directly on top of the embedded cap (due to the higher forces needed to impregnate all of the cap's porosity), and vent holes were located throughout the mold where air was likely to be trapped.

**Fabrication:** Due to the structural complexity and small feature sizes of the bellows, coupled with the required elastomer impregnation of the modified peristaltic pump cap, and the integration of the tubing and wire mesh, the entire appendage assembly was designed to be injection molded. This approach allows for sufficiently high injection pressures on the cartridge gun's pistons (830 kPa/120 PSI) to flow the elastomer through the myriad of small openings and cavities.

As shown in Figure 6A, the white top and bottom molds, soft cores, and rods were first sprayed with Smooth-On Ease Release 200 to allow for ease of removal. The soft cores were also manufactured through a similar injection molding process, but instead used True Skin 30 silicone (CHT Germany GmbH, Tübingen, Germany), which has an elongation to break that is three times that of the bellow's elastomer, thus permitting ease of removal after molding.

During fabrication, the tubing was first inserted into the modified peristaltic pump cap, and a specially designed plug for the soft cores was then inserted into the tubing openings to prevent silicone from entering (Figure 6B). The soft core and cap assemblies were then inserted into the bottom mold. The metal support rods were then inserted through the mold and soft cores, and the locations of the soft cores were adjusted

with tweezers until centering was achieved. The wire mesh was then inserted down the neutral axis as shown in Figure 6C. Finally, the top mold was added and M5 screws with embedded square nuts were used to clamp the mold assembly together (Figure 6D).

The actuator mold assembly was then injected with Smooth-Sil 945, a two-part silicone with a 1:1 mix ratio by weight, and a cured Shore hardness of 45 A. The two unmixed components were loaded into a Nordson EFD 1500 mL cartridge (Nordson EFD, East Providence, RI, USA), degassed, and the cartridge plungers were inserted. The cartridge was then loaded into an Albion AT1500X air-powered cartridge gun (Albion Engineering, Moorestown, New Jersey, USA) and a Nordson EFD Series 480 Optimixer (#7 361 707) static mixing nozzle was attached. The elastomer was then dispensed at 830 kPa (120 PSI) into the gate opening of the mold, as shown in Figure 6, until the material overflowed from the mold vents and air bubbles were no longer observed (which took less than 1 min to perform). The mold was then placed in an oven at 65 °C for 30 min until fully cured. The rods and screws and the top and bottom molds were then removed. Compressed air was blown between the soft core and molded bellows to loosen the soft cores, which were then removed with parallel jaw pliers, through the opening seen in the left of Figure 6E.

To cap the tip of the molded bellow with additional elastomer, a small cap mold was used, as shown in Figure 6. First, the distal opening of the bellow, which was created following removal of the soft core, was cleaned with isopropanol, and the bellow was placed into the cap mold. Two luer lock fittings (for the left and right bellow openings) were screwed into the cap mold, and a syringe filled with mixed Smooth-Sil 945 was inserted into the fittings, while the bellow was oriented vertically, with the mold side facing down. A precise volume (0.75 mL) of silicone (calculated in CAD to completely seal the bellow tips) was then injected into each side of the bellows and capped. The bellow and its associated cap mold was then placed, still hanging in a vertical orientation, into a 65 °C oven for 30 min until fully cured. The cap mold was then removed and the remaining flashing is trimmed, as shown on the right in Figure 6.

Finally, the bellow was filled with water, primarily chosen due to convenience and compatibility for underwater use, but other liquids such as glycerol or vegetable oil could provide different fluidic properties, but which at this point have not been explored. Bellow filling started by inserting 1/8" plastic plugs into the rod holes located under the pump cap (Figure 6F). Two nozzles were next inserted between the top left and top right plugs and holes, and a syringe was used to inject water, while the opposite nozzle allowed air to escape (Figure 6G). Once all of the air had escaped and only water was flowing from the venting nozzle, the venting nozzle was removed. With the plug remaining in place, the syringe was used to further inflate the bellow with an additional 26 mL of water, and when full, the fill nozzle was removed.

**FEM Characterization:** Due to challenges associated with the development of analytical models for accurately simulating the behavior of structurally complex soft actuators<sup>[30–32]</sup> such as the bidirectional design described here, finite element (FE) analysis was instead used to explore the energetic efficiency of the system.

The performance of the bidirectional PneuNet actuator, excluding the pumping system, was investigated using the FE method with the commercial software ABAQUS (Dassault Systèmes). The CAD geometry was imported as a solid and meshed using tetrahedral elements (element type C3D4H), while the thin metal (strain-limiting) mesh was modeled using shell elements (element type S3). The mechanical response of Smooth-Sil 945 Silicone Rubber was captured using an incompressible neo-Hookean material (with an initial shear modulus of 0.32 MPa), whereas the metal mesh was modeled as a linear elastic material with Young's modulus of 2.5 GPa and Poisson's ratio of 0.33. Both chambers of the actuator were converted to fluidic cavities, such that volume control could be imposed as a loading during a dynamic implicit simulation. The loading was applied in two steps. First, both cavities were inflated with a total volume of 26 mL, in accordance with the preloading described in the manufacturing process in Section 3.2. In a second step, volume was moved from the right fluidic chamber to the left fluidic chamber to instigate bending deformation. During loading, the pressure was tracked in each chamber while the

bending performance was assessed by tracking four equidistant points along the actuator's neutral axis, and a least-squares circle was fitted to estimate the bending radius during loading.

In **Figure 7A** the numerical (orange line) and experimental (green line) characteristics of the actuator are compared by plotting the pressure difference between both fluidic chambers as a function of the bending radius. From this analysis it can be concluded that there is a good agreement between experimental and numerical results. As such, the FE analysis can be used as a tool to gain a deeper understanding into the workings of this actuator. In Figure 6C the pressure–volume relation of both the left and right fluidic cavities (note that the unloaded condition for both cavities is indicated by a grey dotted line) is reported. During the preloading step, the input volume is evenly distributed over the two cavities, resulting in an equal increase in pressure and no bending deformation. In contrast, during the second step, the fluid that is moved from the right chamber to the left leads to a separation of PV curves, where the decrease in pressure in the right chamber is far greater than the increase in pressure of the left chamber.

The pressure–volume curves in Figure 6C can be used to determine the energy required to induce actuator bending. The energy needed to bring a fluidic cavity from  $V_1$  to  $V_2$  can be calculated as follows

$$\Delta E = \int_{V_1}^{V_2} p dV \quad (1)$$

which equals the area under the pressure–volume curve of the right and/or left chamber, which is shown in Figure 7D as a function of the input volume of the left chamber. The total energy that needs to be applied to induce actuator bending can be derived by summing up both contributions, where the energy balance was set to zero after preloading the structure (Figure 7E). From these results, it can be concluded that it takes  $\approx 0.426$  J to bend the actuator to a radius of 31.6 mm, which corresponds to the bending deformation shown in the inset of Figure 7A.

**Efficiency:** Soft robot efficiencies are generally poor, ranging from 10% for jumping, 0.1% for swimming, and less than 0.001% for earthworm-like movements.<sup>[33–37]</sup> Dramatically improving these efficiencies is of critical importance for increasing the functional lifespans of untethered soft robots, and the results reported here make significant advances toward achieving this goal.

The efficiency of the total system was characterized from the DC electrical input power to the power required to bend the actuator at a given speed, and to a given radius (or equivalent differential pressure as mapped in Figure 7). Figure 2G shows the methods and measurement points of the system. The efficiency of the total system,  $\eta_t$ , is the product of the efficiency of the controller ( $\eta_{\text{Controller}}$ ), stepper driver ( $\eta_{\text{SD}}$ ), stepper motor ( $\eta_{\text{SM}}$ ), peristaltic pump's mechanical–hydraulic efficiency ( $\eta_{\text{Pump}}$ ), and hydraulic to bending efficiency of the bellow ( $\eta_{\text{Bending}}$ ).

**Efficiency Equations:** The controller's efficiency can be estimated as

$$\eta_{\text{Controller}} = \frac{P_{\text{SD}}}{P_{\text{Controller}}} = \frac{i_{\text{SD}} \cdot V_{\text{SD}}}{i_{\text{Controller}} \cdot V_{\text{Controller}}} \quad (2)$$

where  $i_{\text{SD}}$ ,  $V_{\text{SD}}$ ,  $i_{\text{Controller}}$ , and  $V_{\text{Controller}}$  are the stepper driver's measured current and voltage, and the controller's measured current and voltage. The stepper driver's efficiency can be calculated at a given RPM as

$$\eta_{\text{SD}} = \frac{P_{\text{SM}}}{P_{\text{SD}}} = \frac{i_{\text{SM}} \cdot V_{\text{SM}}}{i_{\text{SD}} \cdot V_{\text{SD}}} \quad (3)$$

where  $i_{\text{SM}}$ ,  $V_{\text{SM}}$ ,  $i_{\text{SD}}$ , and  $V_{\text{SD}}$  are the instantaneous electrical values of the stepper motor's current and voltage, and the stepper driver's current and voltage, over a full step cycle. The efficiency of the stepper motor can be calculated as

$$\eta_{\text{SM}} = \frac{P_{\text{Pump}}}{P_{\text{SM}}} = \frac{T_e \cdot n}{i_{\text{SM}} \cdot V_{\text{SM}}} \quad (4)$$

where  $P_{\text{Pump}}$  is the effective torque ( $T_e$ ) times the angular velocity ( $n$ ), and  $P_{\text{SM}}$  is the instantaneous current ( $i_{\text{SM}}$ ) times the instantaneous voltage

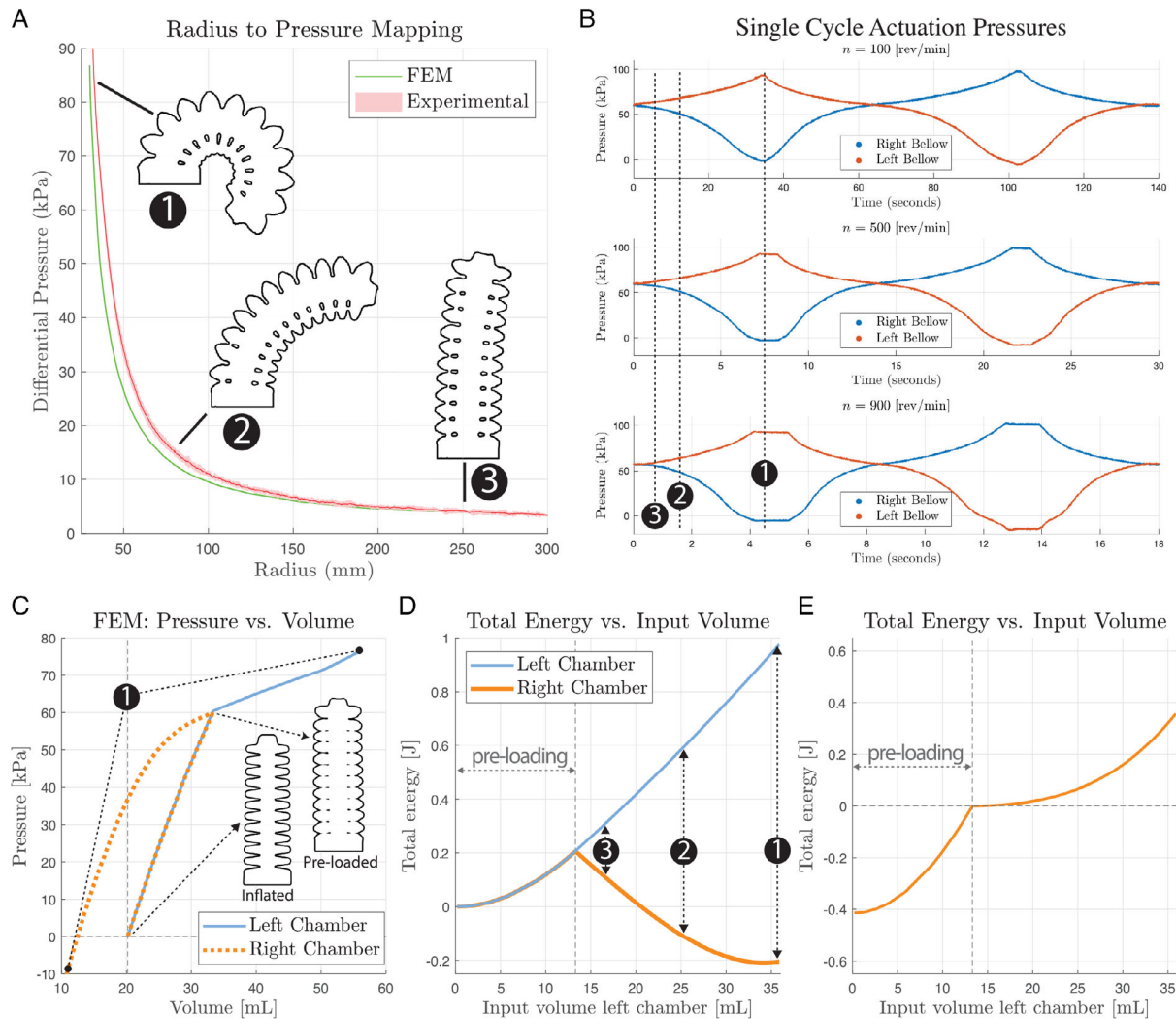


**Figure 7.** Experimental tests and simulations of actuator performance. Actuator images are outlines from FEM simulations at the given point. A) Radius versus differential pressure of the bellow, where the pink shadow of the experimental data averages (red line) represents the  $\pm$  one standard deviation, with five samples at each of the ten motor speeds (10, 100, 200, 300, 400, 500, 600, 700, 800, and 900 RPM). B) Single-cycle actuation pressures and timing for motor speeds at 100, 500, and 900 RPM. The plots represent the actuator starting from an unbent position, with a beginning cycle of bending clockwise (as seen with markers 3, 2, and 1), returning to the unbent position, followed by a cycle bending counterclockwise and returning. C) FEM pressure versus volume for the left and right channels showing inflated, preloaded, and minimum bending radii. D) Total required pumping energy versus input volume for the left and right channels, as observed relative to the left chamber volume. E) Total energy versus input volume for the left chamber.

( $V_{SM}$ ) over a full step cycle. The peristaltic pump's volumetric efficiency can be defined as

$$\eta_v = \frac{Q_e}{Q_{th}} = \frac{Q_e}{D \cdot n} \quad (5)$$

which addresses the flow losses of the pump's theoretical flow rate ( $Q_{th}$ ) to the effective flow rate ( $Q_e$ ), where  $D$  is the pump's displacement and  $n$  is the shaft's angular velocity. The peristaltic pump's mechanical-hydraulic efficiency ( $\eta_{Pump}$ ) can be defined as

$$\eta_{Pump} = \frac{P_{Hyd}}{P_{Pump}} = \frac{Q_e \cdot \Delta p}{T_e \cdot n} = \eta_v \cdot \eta_{mh} \quad (6)$$

which is a function of the hydraulic power divided by the pump's mechanical power.

The efficiency of the bellow actuator can be calculated as follows

$$\eta_{bending} = \frac{P_{Bending}}{P_{Hyd}} \quad (7)$$

where  $P_{Bending}$  is computed from the energy in the FE analysis to bend the actuator to a specified radius over a given time, and mapped to the RPM of the stepper motor. The total system efficiency can be thus calculated as

$$\eta_t = \eta_{Controller} \cdot \eta_{SD} \cdot \eta_{SM} \cdot \eta_{Pump} \cdot \eta_{Bellow} \quad (8)$$

**Experimental Setup:** To understand the global efficiency of the system, the efficiencies of each of the individual components were analyzed. The controller used to drive the stepper motor and execute motion commands was a Duet 2 Wifi (Duet 3D, UK), which uses high-efficiency TMC2660 stepper drivers (Trinamic, Hamburg, Germany), which were configured for full

steps, with a maximum current of 1000 mA. Acceleration control was turned off (resulting in the maximum possible acceleration), and a 24 V DC power supply was used to supply power to all electronics through the Duet 2 WiFi.

$P_{\text{controller}}$ ,  $P_{\text{SD}}$ , and  $P_{\text{SM}}$  were measured with a Keysight DSOX3 oscilloscope (Santa Rosa, CA, USA), equipped with Tektronix A622 (Beaverton, OR, USA) current and voltage probes. Adjacent subsystems were measured simultaneously to ensure the chopper drive signal of the stepper driver and stepper motor were synchronized.  $P_{\text{pump}}$  was measured in situ between the pump head and the stepper motor with a noncontact rotary torque sensor and encoder (Futek Model #TRH605, Irvine, CA, USA), and recorded with a National Instruments USB-6002 DAQ (Austin, TX, USA).  $P_{\text{Hyd}}$  was measured using analog pressure gauges and a graduated cylinder over a range of pressures and RPMs.  $P_{\text{Bending}}$  was measured with a Vicon MX-GIGANET, six T040  $f=18$  mm/F2 tracking cameras, and Vicon Tracker v3.7.0 software (Vicon Motion Systems Ltd, UK) using five markers spaced evenly down the neutral axis of the bellow. Differential pressure was measured using two ProSense pressure transmitters (Model #SPT25-10-V30D, Oosterhout, The Netherlands) inserted in the integrated peristaltic pump head, and recorded with a USB-6002 DAQ synchronized with the Vicon system.

## Supporting Information

Supporting Information is available from the Wiley Online Library or from the author.

## Acknowledgements

The authors gratefully acknowledge support from the Office of Naval Research (award No. N00014-17-1-2063) and the Wyss Institute for Biologically Inspired Engineering.

## Conflict of Interest

The authors declare no conflict of interest.

## Data Availability Statement

The data that support the findings of this study are available from the corresponding author upon reasonable request.

## Keywords

biomimetic robots, fluidic engine, modular soft actuators, pneunet, soft locomotion, soft manipulation

Received: May 13, 2021  
Revised: August 10, 2021  
Published online:

- [1] R. F. Shepherd, F. Ilievski, W. Choi, S. A. Morin, A. A. Stokes, A. D. Mazzeo, X. Chen, M. Wang, G. M. Whitesides, *Proc. Natl Acad. Sci.* **2011**, *108*, 51 20400.
- [2] M. T. Tolley, R. F. Shepherd, B. Mosadegh, K. C. Galloway, M. Wehner, M. Karpelson, R. J. Wood, G. M. Whitesides, *Soft Robotics* **2014**, *1*, 213.
- [3] M. T. Tolley, R. F. Shepherd, M. Karpelson, N. W. Bartlett, K. C. Galloway, M. Wehner, R. Nunes, G. M. Whitesides, R. J. Wood, in *IEEE Int. Conf. on Intelligent Robots and Systems*, IEEE, Piscataway, NJ **2014** pp. 561–566.

- [4] H.-Y. Chen, R. S. Diteesawat, A. Haynes, A. J. Partridge, M. F. Simons, E. Werner, M. Garrad, J. Rossiter, A. T. Conn, *Front. Robot. AI* **2019**, 6.
- [5] Y. Zhang, L. Ge, J. Zou, H. Xu, G. Gu, in *2019 IEEE/RSJ Int. Conf. on Intelligent Robots and Systems (IROS)*. IEEE/RSJ, Macau, **2019**, pp. 3343–3348.
- [6] M. Bell, I. Pestovski, W. Scott, K. Kumar, M. Jawed, D. Paley, C. Majidi, J. Weaver, R. Wood, *IEEE Robot. Automat. Lett.* **2018**, *3*, 3.
- [7] M. Bell, T. Paschal, J. Sperry, S. Sieniewicz, R. Wood, J. Weaver, *IEEE Robot. Automat. Lett.* **2019**, *4*, 4.
- [8] M. A. Bell, L. Cattani, B. Gorissen, K. Bertoldi, J. C. Weaver, R. J. Wood, in *IROS 2020, IEEE/RSJ International Conference on Intelligent Robots and Systems (IROS)*, Las Vegas, NV, USA **2020**, 6529, <http://doi.org/10.1109/IROS45743.2020.9341138>.
- [9] P. Boyraz, G. Runge, A. Raatz, *High-Throughput* **2018**, *7*, 3.
- [10] C. D. Onal, D. Rus, *Bioinspir. Biomimet.* **2013**, *8*, 2.
- [11] M. Luo, Y. Pan, E. H. Skorina, W. Tao, F. Chen, S. Ozel, C. D. Onal, *Bioinspir. Biomimet.* **2015**, *10*, 5.
- [12] V. W. Oguntosin, S. J. Nasuto, Y. Hayashi, in *Proc. - UKSim-AMSS 17th Int. Conf. on Computer Modelling and Simulation, UKSim 2015*. IEEE, Piscataway, NJ **2016**, pp. 242–247.
- [13] Z. Zhang, X. Wang, S. Wang, D. Meng, B. Liang, *IEEE Access* **2019**, *7* 134301.
- [14] Z. Shen, J. Na, Z. Wang, *IEEE Robot. Automat. Lett.* **2017**, *2*, 2217.
- [15] T. Hainsworth, L. Smith, S. Alexander, R. MacCurdy, *IEEE Robot. Automat. Lett.* **2020**, *5*, 4118.
- [16] R. K. Katzschmann, A. D. Marchese, D. Rus, in *Springer Tracts In Advanced Robotics*, Vol 109, Springer Verlag, Berlin, **2016**, pp. 405–420.
- [17] A. D. Marchese, C. D. Onal, D. Rus, *Exper. Robot.* **2013**, 41.
- [18] A. D. Marchese, C. D. Onal, D. Rus, *Soft Robot.* **2014**.
- [19] A. D. Marchese, R. K. Katzschmann, D. Rus, *Soft Robot.* **2015**, *2*, 7.
- [20] A. D. Marchese, D. Rus, *Int. J. Robot. Res.* **2016**, *35*, 840.
- [21] D. Rus, M. T. Tolley, *Nature* **2015**, *521*, 467.
- [22] M. Wehner, M. T. Tolley, Y. Mengüç, Y.-L. Park, A. Mozeika, Y. Ding, C. Onal, R. F. Shepherd, G. M. Whitesides, R. J. Wood, *Soft Robot.* **2014**, *1*, 263, <http://doi.org/10.1089/soro.2014.0018>.
- [23] K. C. Galloway, K. P. Becker, B. Phillips, J. Kirby, S. Licht, D. Tchernov, R. J. Wood, D. F. Gruber, *Soft Robot.* **2016**, *3*, 23.
- [24] D. Padovani, E. J. Barth, *IEEE Int. Conf. on Soft Robotics (RoboSoft)*, New Haven, CT, USA, **2020**, 345, <http://doi.org/10.1109/RoboSoft48309.2020.9116049>.
- [25] P. Polygerinos, Z. Wang, K. C. Galloway, R. J. Wood, C. J. Walsh, in *Robotics And Autonomous Systems*, Vol. 73, Elsevier, Amsterdam **2015**, pp. 135–143.
- [26] P. Polygerinos, K. C. Galloway, E. Savage, M. Herman, K. O. Donnell, C. J. Walsh, in *Int. Conf. on Robotics and Automation (ICRA)*, 2015, Seattle, WA, USA **2015** pp. 2913–2919, <http://doi.org/10.1109/ICRA.2015.7139597>.
- [27] M. Adami, A. Seibel, *On-Board Pneumatic Pressure Generation Methods for Soft Robotics Applications*, **2019**, *8*, 2, <https://doi.org/10.3390/act8010002>.
- [28] Y. Kim, Y. Cha, *Front. Bioeng. Biotechnol.* **2020**, 8.
- [29] M. Bryant, J. Fitzgerald, S. Miller, J. Saltzman, S. Kim, Y. Lin, E. Garcia, in *Active and Passive Smart Structures and Integrated Systems 2014* Vol. 9057, SPIE, San Diego, California, United States **2014**, p. 90570H, <https://doi.org/10.1117/12.2046368> (accessed: March 2014).
- [30] B. Gorissen, W. Vincentie, F. Al-Bender, D. Reynaerts, M. De Volder, *J. Micromech. Microeng.* **2013**, *23*, 4.
- [31] G. Gu, D. Wang, L. Ge, X. Zhu, *Soft Robot.* **2020**, *8*, 462, <http://doi.org/10.1089/soro.2020.0039>.

- [32] Z. Zhang, Q. Zhang, M. Dai, X. Ding, Z. Xia, *24th Inter. Conf. on Mechatronics and Machine Vision in Practice (M2VIP)* Auckland, New Zealand **2017**, 1, 10.1109/M2VIP.2017.8211482.
- [33] L. Shui, L. Zhu, Z. Yang, Y. Liu, X. Chen, *Soft Matter* **2017**, 13, 8223.
- [34] S. I. Rich, R. J. Wood, C. Majidi, *Nat Electron*, **2018**, 1, 102.
- [35] L. Chen, Y. Xue, W. Chen, M. Zhang, X. Chen, X. Cao, Z. Zhang, G. Li, T. Li, *J. Appl. Phys.* **2018**, 124, 16.
- [36] L. Zhu, Y. Cao, Y. Liu, Z. Yang, X. Chen, *Soft Matter* **2017**, 13, 4441.
- [37] T. Ren, Y. Li, M. Xu, Y. Li, C. Xiong, Y. Chen, *Soft Robot.* **2020**, 7, 130.